Comparison of actuator line modelling of tidal power kites with ADCP observations

Nimal Sudhan Saravana Prabahar, Sam Fredriksson, Göran Broström, Björn Bergqvist

Abstract—**The Deep Green (DG) power plant which is based on a tethered kite model aims to operate efficiently in tidal current velocities as low as 1.2 m/s. In a previous project, numerical modelling of the Deep Green in a tidal flow was carried out using Large Eddy Simulations (LES) and Actuator Line Method (ALM) implemented in the OpenFOAM solver. In this study, results from the numerical model have been compared to Acoustic Doppler Current Profiler (ADCP) observations taken in the wake of a Deep Green under similar conditions. A direct comparison of the data showed that the numerical model data needs to be resampled in a similar way that the ADCP would measure and process data using a virtual ADCP. The effect of the Deep Green on the tidal flow is analysed using the numerical model and the observations by comparing the instantaneous and time-averaged stream velocities. After resampling, the numerical model and observations show good agreement. This suggests that the numerical model can be used for further analysis such as array studies etc. Further, whilst making ADCP observations in tidal turbine wakes, the parameters of the instrument, especially the orientation of the beams, bin/cell size, and pulse lengths have a significant impact on the level of detail in the observed velocity profile.**

Keywords— **tidal turbines, ADCP, actuator line method, deep green, tidal power kites.**

I. INTRODUCTION

TIDAL power has an increasing possibility to be a part of future renewable energy systems. The tides dissipate approximately 3.7 TW of energy globally [1], however, only a small fraction of it is available for power generation. Tidal turbines are one of the methods to harness power from tidal flows [2]. Sharing similarities in operation with wind turbines, these tidal turbines require strong tidal flows to function efficiently [3]. The Deep Green (DG) power plant is a kite-borne tidal power generator, that aims to operate efficiently in low-velocity tidal flows. DG500, the power plant used in this study, consists of a 12 m wing that is anchored to the sea floor using a tether (see Fig. 1(a)). The turbine is mounted on a nacelle attached to the wing. The nacelle houses the generator, and the power electronics and the power is

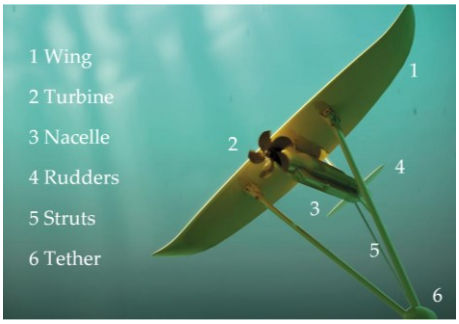

Fig. 1(a). Deep Green power plant (wing, nacelle, turbine, sturts, rudders) – reprint from Minesto AB.

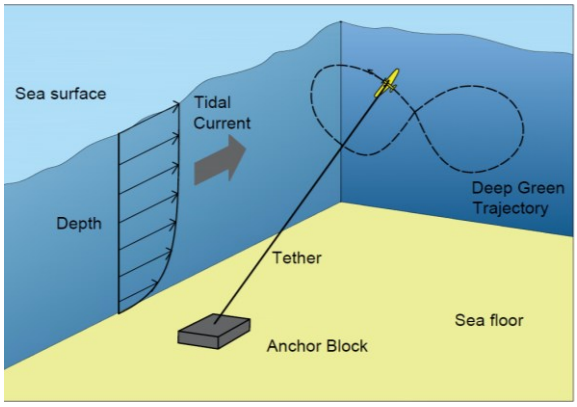

Fig. 1(b). Deep Green operation in a tidal flow

We acknowledge funding from Swedish Energy Agency through the project P42247-2. The computations were enabled by resources provided by the Swedish National Infrastructure for Computing (SNIC) at C3SE and NSC partially funded by the Swedish Research Council through grant agreements no. SNIC 2020/1-32, SNIC2019-1-42 and SNIC2018-1-42.

Nimal Sudhan Saravana Prabahar (e-mail: nimal.sudhan.saravana.prabahar@gu,se), Sam Fredriksson (e-mail: sam.fredriksson@marine.gu.se), and Göran Broström (e-mail: goran.brostrom@marine.gu.se) are affiliated to the Department of Marine Sciences, University of Gothenburg, Box 46, SE-405 30, Gothenburg, Sweden. Sam Fredriksson is also affiliated to the Swedish Meteorological and Hydrological Institute, Sven Källfelts gata 15, SE-426 71, Gothenburg, Sweden. Björn Bergqvist (email: bjorn.bergqvist@minesto.com) is a concept group manager at Minesto AB, Gothenburg, Sweden.

Digital Object Identifier: https://doi.org/10.36688/ewtec-2023-544

transmitted via the tether. Using control systems and four rudders, the DG is steered in a lemniscate trajectory (∞), mostly perpendicular to the tidal flow (see Fig. 1(b)). As the turbine follows the lemniscate trajectory, the relative velocity through the turbine is 5-10 times the tidal flow velocity. The lemniscate trajectory has a horizontal width of 64 m and a vertical dimension of 22 m. The studied site for DG500 is Holyhead, on the coast of Wales where the depth is 80 m. The DG500 has a rated power of 500 kW.

Numerical modelling of tidal turbines has been similar to the methods used for wind turbines. Such numerical models use either low-fidelity methods such as analytical wake models [4, 5] or high-fidelity methods using Computational Fluid Dynamics (CFD) [6-9] or a combination of both depending on the nature of the study. Validating numerical models against field observations or scaled model measurements can increase their redundancy. For wind turbines, extensive validation studies have been conducted [10-13], however for tidal turbines, there exists a lesser number of validation studies [14, 15]. Further, numerical models and validation studies for tidal turbines lacked coverage of kite-borne turbines so far. Fredriksson et al. [16, 17] developed a numerical model for tidal power kites using Large Eddy Simulations (LES) and Actuator Line Method (ALM). In this study, results from this numerical model is compared to Acoustic Doppler Current Profiler (ADCP) observations from the testing of DG500 by Minesto AB. The observations were done using a vessel mounted ADCP located 70 m downstream of the DG trajectory at Holyhead.

A. Abbreviations and acronyms

ADCP	Acoustic Doppler Current Profiler
vADCP	virtual Acoustic Doppler Current Profiler
ALM	Actuator Line Model
DG	Deep Green
LES	Large Eddy Simulations
δx	x distance relative to DG trajectory centre (positive downstream)
δy	y distance relative to DG trajectory centre

B. Coordinate systems and velocities

(x, y, z)	Numerical model coordinate system
(u, v, w)	Spatially filtered velocities in the numerical model coordinate system
(x_o, y_o, z_o)	Observation coordinate system
(u_o, v_o, w_o)	Velocities in the observation coordinate system
(u_r, v_r, w_r)	Resampled model velocities using a virtual ADCP

II. Methodology

A. Numerical Model

The numerical model developed by Fredriksson et al. [16, 17] is based on the turbinesFOAM library of OpenFOAM [18] that has been modified to include arbitrary blade/wing trajectories. LES uses spatially filtered Navier-Stokes and continuity equations, resolving the eddies larger than a set dimension and modelling the smaller ones using a single equation eddy-viscosity model [19, 20]. The tidal cycle is simulated using a sinusoidal momentum source with a time period of 12 hours. A precursor analysis was done to obtain a fully developed and turbulent initial condition, and further details regarding the precursor can be obtained from Fredriksson et al., [16, 17].

The numerical model follows a cartesian coordinate system with spatially filtered velocities u, v, and w in axes x, y, and z (see Fig. 2). x is the stream direction, y is the cross stream, and z is the vertical direction. A domain size of 600 m × 240 m × 80 m in the x, y, and z directions is used. A uniform grid size of 0.625 m is chosen with 960, 384, and 128 cells in the x, y, and z directions (47,185,920 cells). The inlet flow is set with a time-varying inlet velocity field captured from the precursor. Cyclic boundary conditions are applied to the side boundaries and this resembles an infinite replication of the domain in the y direction. A rigid lid is used as a top boundary with slip boundary conditions. Scans of the test site revealed boulders of size 1-3 m on the sea floor at a frequency of 1.6 per 100m x 100 m, therefore the bottom boundary is modelled as a rough wall with a roughness height of 0.01 m. Instead of resolving the flow near the rough wall, wall functions are used, which correct the turbulent viscosity near the wall to account for wall roughness (done using OpenFOAM nutkRoughWallFunction).

Including the DG geometry in the domain will be computationally expensive as it would demand a finer grid near the wing and moving meshes. Instead, the DG is modelled using momentum source terms applied to the regions of influence of the DG using Actuator Line Method (ALM) [8, 21]. The DG wing is split into finite span-wise elements and the force in each element i is computed as,

$$\mathbf{f}_i = \frac{1}{2}\rho U_{r,i}^2 C_i l_i \left(C_{L,i}\mathbf{e}_{L,i} + C_{D,i}\mathbf{e}_{D,i}\right), \quad (1)$$

where, $U_{r,i}$ is the relative flow velocity between the element and the free stream, C_i and l_i are the chord and span of the element. $C_{L,i}$ and $C_{D,i}$ are precomputed lift and drag coefficients in the directions $\mathbf{e}_{L,i}$ and $\mathbf{e}_{D,i}$. The force $\mathbf{f}_i$ is applied on the grid points within a Gaussian sphere of influence of the wing element using (2). $\mathbf{f}_{DG,i}$ is the DG force applied to the computational grid.

$$\mathbf{f}_{DG,i}\left(\mathbf{e}_{r,i}\right) = \frac{\mathbf{f}_i}{\varepsilon^3 \pi^{\frac{3}{2}}} \exp\left[-\left(\frac{\left|\mathbf{e}_{r,i}\right|}{\varepsilon}\right)^2\right]. \quad (2)$$

In (2) $\mathbf{e}_{r,i}$ is the vector from the grid point to the centre of the wing element and ε is the width of the Gaussian sphere.

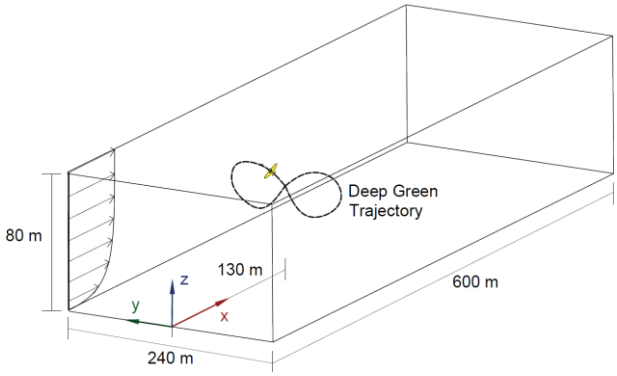

Fig. 2. Computational domain used in the numerical model with the Deep Green trajectory and coordinate system shown.

The simulation is performed in OpenFOAM using a finite volume method (pimpleFOAM solver). A second-order implicit backward scheme is used for time discretization: using current and two previous time steps. Advection and diffusion terms are discretized using a blend of 98 % second-order linear and 2 % first-order upwind schemes [17]. A time step of 0.1 seconds is used.

B. ADCP observations

The ADCP used was Teledyne RD Instruments Workhorse broadband ADCP (307.2 kHz) with a sampling frequency of 0.455 Hz. The vessel mounted ADCP recorded data for 6.5 hours covering half of the tidal cycle at Holyhead. Cell/Bin size was set as 4 m. The coordinate system used for the observations is x_o, y_o, and z_o as the stream, cross stream, and vertical directions respectively, and the corresponding velocity components u_o, v_o, and w_o. ADCP data is processed using Teledyne Instruments WinADCP software to obtain the beam and earth velocity components. The DG was operational for 15 minutes at around 10:10 UTC on August 30, 2018.

C. Resampling methodology of the virtual ADCP

1) ADCP working principles

ADCP uses a transducer to send a receive sound pulses and the flow speed parallel to the pulse is estimated using the Doppler shift in the frequency as,

$$b = {}^{f_d c}/_{2f_s}, \tag{3}$$

where b is the relative flow speed parallel to the sound wave. f_s and f_d are the frequencies of the sound wave and the Doppler shift respectively, and c is the speed of sound in water [22]. Since the transducer measures the component of flow parallel to the beam, to obtain the 3-D flow components, a minimum of 2 pairs of sound beams oriented in different directions are needed as seen in Fig. 3(a) [23, 24]. Velocity components from the four beams are used to compute the stream, cross-stream, and vertical velocities. Further, the ADCP recordings are averaged over a depth range and the entire observation depth is divided into cells/bins with size l_{bin}. A sound

TABLE I
ADCP BEAM ORIENTATION RELATIVE TO THE NUMERICAL MODEL AND OTHER ADCP PARAMETERS

Beam	Transducer width [m]	Beam width [deg]	Beam elevation, β [deg]	Assumed beam direction vector
1	0.09	3.7	20	[-0.2418, -0.2418, -0.9397]
2	0.09	3.7	20	[0.2418, 0.2418, -0.9397]
3	0.09	3.7	20	[-0.2418, 0.2418, -0.9397]
4	0.09	3.7	20	[0.2418, -0.2418, -0.9397]

Transducer width is the diameter of the transducer. Beam elevation, β, is the angle of the beam relative to the vertical direction. This beam orientations are *assumed* since the exact orientation during the observations is not known. Further the pulse length is *assumed* to be same as the cell size of 4m

pulse of length l_{pulse} is transmitted from the transducer. Then the transmitter starts to receive signals from each bin by opening and closing of time gates corresponding to the bin [22]. Though the observations are averaged over a range, the values closer to the bin centre are given higher weightage as discussed below. The transducer starts receiving when sufficient time has passed to let the head of the pulse reach a particular bin's centre and scatter back to the transducer. At the same instant, the signal received by the transducer will also contain the scatters from other parts of the pulse, which have not reached the bin centre yet. Since the transducer will be receiving until the pulse tail leaves the bin centre, the transducer continuously receives scatters along the pulse. Hence the (averaged) range where the velocity is measured equals l_{pulse} on either side of the bin centre. The portion of signals from the bin centre will, however, be higher than from the bin boundaries.

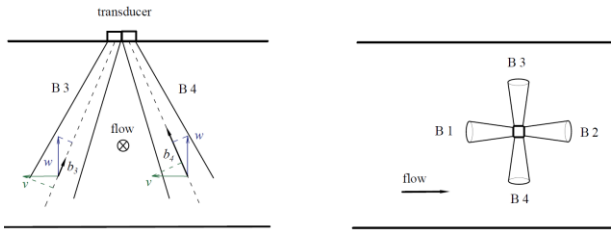

Fig. 3(a). ADCP beam orientations to observe the 3 D velocity components (u, v, and w). b_1, b_2, b_3, and b_4 are the relative flow speed measured by beams B1, B2, B3, and B4.

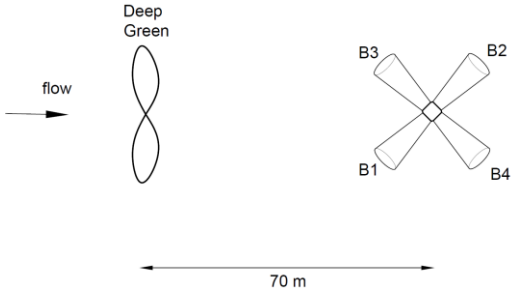

Fig. 3(b). Assumed ADCP beam orientations during the observations (top view). Refer Table. 1 For further details.

In Fig. 3(a), the angle of the beam with the vertical, β, is 20 degrees. Hence, the beams diverge away from each other as the depth increases. For studying the DG wake the orientation of the beam with the flow direction is critical as it influences which regions of the wake are measured. In ship-mounted ADCPs, the common practice is to rotate the beams 45 degrees in the vertical axis, such that there is minimum interference with the ship's wake. So, in these observations, an assumption is made that the beams are rotated 45 degrees in the vertical axis (see Fig. 3(b)). Whilst measuring large-scale features such as the tidal flow, the orientation would be of less significance, but it has a larger impact here. The assumed beam orientations and other parameters are given in Table 1.

2) vADCP resampling methodology

If the ADCP velocities are compared directly with numerical model data taken 70 m downstream of the DG, there will be discrepancies in the structure of the wake. The velocities from the numerical model are measured at exactly $\delta x = 70, \delta y = 0$ (δx and δy are the relative distance from the DG trajectory centre in x and y directions, δx positive is downstream). However, the region measured by the ADCP expands as the distance between the beams increases with the depth (see Fig. 3(a) & (b)) reaching up to 60 m. Hence, to have a similar comparison, the numerical model results are resampled with a virtual ADCP (vADCP) in the domain at the same location relative to the DG. The resampling methodology is as follows.

The instantaneous velocity field is captured at the same sampling frequency of the ADCP (0.455 Hz) from the numerical model. In the computational domain, the grid points that fall within the induvial beams of the vADCP are filtered by assuming the beams as cones. For a point to be inside the cone (beam), the angle between the vector from the grid point to the cone apex ($\mathbf{e}_m$) and the axis of the cone ($\mathbf{e}_b$) should be less than half of the beam angle (α). The filter function, γ is 1 if the point is inside and 0 if its outside, is defined as,

$$\gamma = \begin{cases} 1 & if \quad cos^{-1}\left(\dfrac{\mathbf{e}_m \cdot \mathbf{e}_b}{|\mathbf{e}_m|\,|\mathbf{e}_b|}\right) \le \dfrac{\alpha}{2} \\ 0 & if \quad cos^{-1}\left(\dfrac{\mathbf{e}_m \cdot \mathbf{e}_b}{|\mathbf{e}_m|\,|\mathbf{e}_b|}\right) > \dfrac{\alpha}{2} \end{cases}. \tag{4}$$

At the filtered grid points the velocity component parallel to each beam, b_n, is computed using,

$$b_n = \left| \left(\frac{(u, v, w) \cdot \mathbf{e}_{b,n}}{\left|\mathbf{e}_{b,n}\right|^2} \right) \mathbf{e}_{b,n} \right|, \tag{5}$$

where, n denotes the beam number (1, 2, 3, and 4) and $\mathbf{e}_{b,n}$ is the direction vector of the beam n. (u, v, w) is the velocity vector in the numerical model. b_n is a scalar as a function of x, y, and z in the numerical model coordinates. In each beam space, b_n with the same z ordinate are spatially averaged in x and y. While vertical averaging into cells, the values closer to the cell centre are given a higher weight than the values away from it [22]. In the vADCP, it is modelled using a linear weight function,

$$\varphi = \begin{cases} \dfrac{z - z_{bin}}{l_{pulse}} + 1 & if \quad z_{bin} - l_{pulse} \le z \le z_{bin} \\ -\dfrac{z - z_{bin}}{l_{pulse}} + 1 & if \quad z_{bin} + l_{pulse} \ge z > z_{bin} \\ 0 & otherwise \end{cases}, \tag{6}$$

where z_{bin} is the z ordinate of the particular bin centre and φ is the weight function at each z ordinate. The exact l_{pulse} value used during the observations is unknown, and the default value is the same as the cell size. Hence the l_{pulse} is assumed to be 4 m in the vADCP. Due to the finite nature of the grid, there might be lesser z values (grid points) on one side of the bin centre than the other. Hence, φ is normalized to maintain the same weight above and below the cell as,

$$\Phi = \begin{cases} \dfrac{\varphi * N}{2 * \sum \varphi\{z \le z_{bin}\}} & if \quad z \le z_{bin} \\ \dfrac{\varphi * N}{2 * \sum \varphi\{z > z_{bin}\}} & if \quad z > z_{bin} \end{cases}. \tag{7}$$

Using the normalized weight function, Φ, the velocities are averaged as,

$$\langle b_n \rangle = \frac{b_n \Phi}{N}, \tag{8}$$

where, $\langle b_n \rangle$ is the cell averaged speed in the direction of the beam n and N is the total number of b_n values. Using the $\langle b_n \rangle$ values from each beam, the 3-D velocity components can be estimated using (9) [22, 23, 24].

$$\begin{aligned} u_a \sin(\beta) + w_a \cos(\beta) &= \langle b_1 \rangle \\ -u_a \sin(\beta) + w_a \cos(\beta) &= \langle b_2 \rangle \\ v_a \sin(\beta) + w_a \cos(\beta) &= \langle b_3 \rangle \\ -v_a \sin(\beta) + w_a \cos(\beta) &= \langle b_4 \rangle. \end{aligned} \tag{9}$$

The subscript a in equation (9) indicates that the velocities are in the beam directions. Using (10), these velocities are transformed into the numerical model coordinate system by rotating in the vertical direction.

$$\begin{bmatrix} u_r \\ v_r \\ w_r \end{bmatrix} = \begin{bmatrix} \cos(45) & -sin(45) & 0 \\ sin(45) & cos(45) & 0 \\ 0 & 0 & 1 \end{bmatrix} \begin{bmatrix} u_a \\ v_a \\ w_a \end{bmatrix}. \tag{10}$$

In (10), the resampled velocities are indicated with a subscript r, and they are in the numerical model coordinate system. u_r, v_r, and w_r are the resampled velocities in the stream, cross-stream, and vertical directions respectively.

III. RESULTS AND DISCUSSION

A. Numerical model

Some results from the numerical model are presented in this subsection without the resampling to understand the effect of the DG on the flow. In Fig. 4(a), results from the numerical model with the DG in the domain is shown as grey iso-surfaces of vorticity magnitude (vorticity = $\nabla \times (u, v, w)$) greater than 0.25. The DG is shown as a blue iso-surface of the magnitude of DG forces. The DG impacts the flow by increasing vorticity downstream. Strong tip vortices generated by the DG wing are seen to follow the lemniscate trajectory and are advected downstream by the tidal flow. The vortices are periodic and structured in the immediate wake of the DG and break up further downstream (see Fig. 4(a)). Velocity reduction by the DG compared to the free stream is represented using the time-averaged stream velocity, $\bar{u}$, in Fig. 4(b). The vertical profiles in the DG wake are plotted in the immediate wake of the DG, at δx = 5 m and two different δy, 0, and 15 m. The former is the trajectory centre, and the latter is the y ordinate where the trajectory is widest in z. In the δy = 0 m, the reduction in velocity is significant compared to the free stream in the trajectory and is increased in the regions outside the trajectory. Since the DG acts as a drag force on the flow, some fluid will move around the DG increasing the velocity in these regions. Two regions of velocity deficit are seen in the δy = 15 m plot, and this corresponds to the centre of one lobe of the lemniscate. Hence, a reduction is seen in the region where the DG passes through. The velocity reduction in δy = 15 m is significantly lesser than the δy = 0 m plot, this is because the DG passes through the centre twice every cycle.

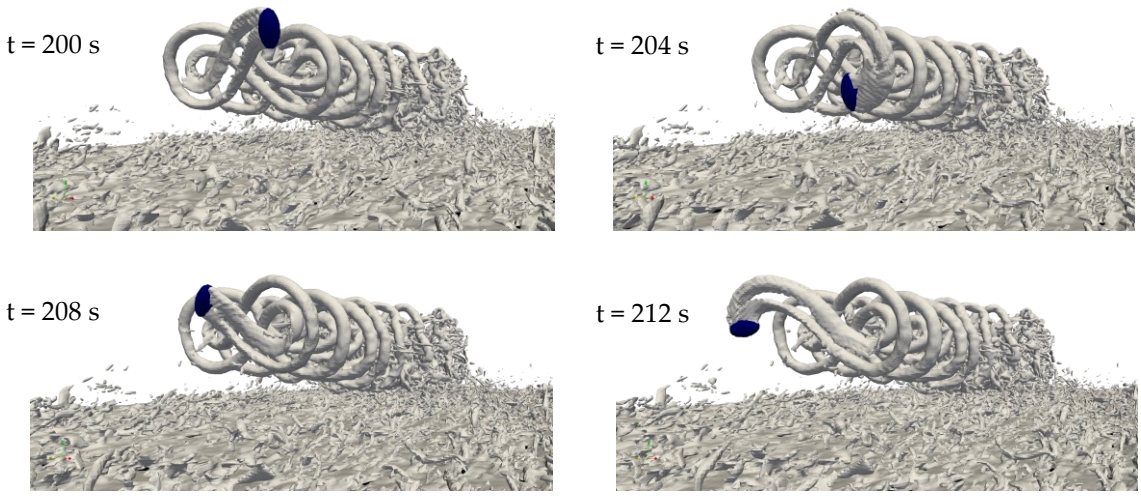

Fig. 4(a). Results from the LES model at different time steps. Grey iso-surface is the magnitude of vorticity greater than 0.25. Blue iso-surface is the magnitude of the DG forces. x, y, and z is location of the numerical model coordinate system.

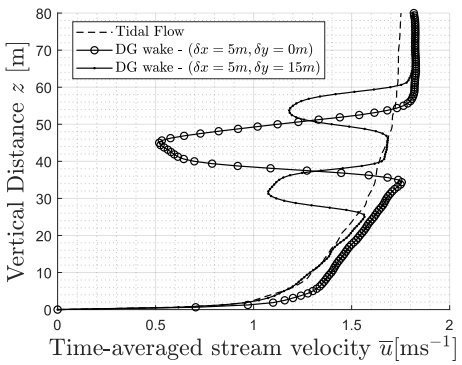

Fig. 4(b). Results from the LES model. Comparison of vertical profiles of time-averaged stream velocity, $\bar{u}$, for the tidal flow and the immediate DG wake. δx and δy are the relative distance from the DG trajectory centre in x and y directions, and positive δx is downstream of the DG.

B. ADCP observations

The stream velocity component from the observations, u_o is represented as a contour plot in Fig. 5. Both the accelerating and decelerating phases of the tidal flow were captured by the ADCP. The peak tidal velocity occurs at around 11:00 and the velocity is in the opposite direction at the start and end of the observations. The flow velocity in the depths the DG operates is higher than 1.5 ms^{-1} over a significant sector of the observations (see Fig. 5). This indicates that the DG could theoretically operate effectively in the tidal cycle in this region. As mentioned, the DG was operational for 15 minutes, 1 hour before the tidal peak. The effect of this could be seen in the observations as a reduction in the stream velocity (see the white square in Fig. 5). It can be observed that the reduction is about 50 percent in a short interval of time. The operation of DG for a longer time can influence the stream velocity on diurnal scales.

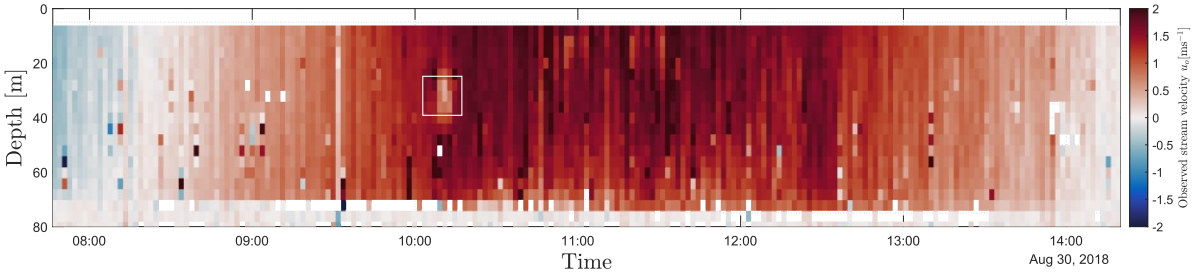

Fig. 5. Stream velocity component, u_o, from the entire ADCP observations. Encircled regions is the velocity reduction caused by the Deep Green operation.

C. *Comparison of the vADCP velocities with the ADCP observations*

Using the vADCP the resampled stream velocity component from the numerical model is plotted in Fig. 6(a) as a function of time. The observed velocity is plotted in Fig. 6(b). The periodic nature of the DG wake is seen in both the numerical model and the observations. There are periods of low velocity when the DG passes through followed by periods of increased velocity. As the DG passes through, some fluid is deflected at a higher velocity thereby increasing the velocity in those regions. In Fig. 6(b), there are two deficit cores at different depths, indicating that the ADCP is not measuring at the trajectory centre due to the diverging beams, although it is located at the trajectory centre. A similar pattern is also seen in the numerical model data indicating that the vADCP is sufficient in capturing data similar to the ADCP. The time period of the DG trajectory is 20 seconds, which is also seen in the wake plots in both the observation and the numerical model.

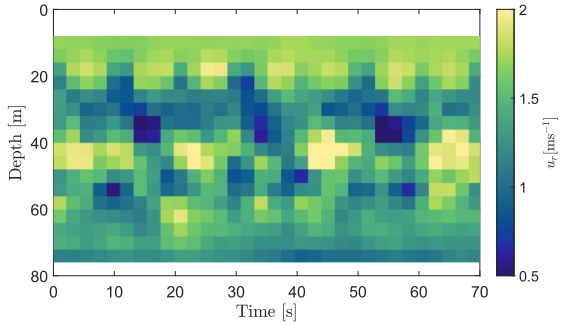

Fig. 6(a). Resampled numerical model stream velocity, u_r, from the vADCP located at $\delta x = 70\ m$.

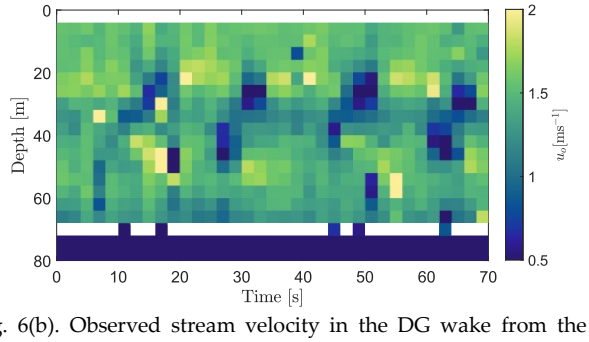

Fig. 6(b). Observed stream velocity in the DG wake from the ADCP, u_o, at $\delta x = 70\ m$.

To further understand the effects of the DG, the stream velocity is time-averaged for 200 seconds. Fig. 7(a) shows the time-averaged stream velocity of the ADCP observations and the LES model for the tidal flow. Since the tide is in the accelerating phase, the tidal velocity profile when the DG is operational is unknown. Hence, it is interpolated from velocity profiles 200 seconds before and after the DG operation. The tidal flow is weaker in the observations than in the numerical model although both are in the same tidal phase.

The DG wake measured by the ADCP and the LES model's vADCP is compared in Fig. 7(a). In the observations, the operation of DG reduced the flow velocity by 25 percent in the trajectory at 70 m downstream (see Fig. 7(a) & (b)). In the numerical model, the velocity deficit is stronger than in the observations. One of the reasons could be the increased tidal flow velocity in the LES model (see Fig. 7(a)). The DG force is proportional to the velocity squared. Neglecting viscous and pressure effects, the deficit velocity can be approximated to be proportional to the square root of the DG forces [25]. Hence a stronger tidal flow can cause a proportionally stronger velocity deficit. Running the numerical model with a lower tidal flow was not possible currently as the DG trajectory data is for a higher tidal flow. The trajectory data derived for one flow can cause force imbalances if used for a different flow.

LES data without resampling is also plotted in Fig. 7(b) at the same location as the vADCP. The velocity profile without resampling does not correlate well with the ADCP observations. The deficit is significantly stronger and at a much lower depth.

The vADCP uses an assumed pulse length (l_{pulse}) of 4m and increasing it will result in smoother velocity profiles. A similar plot to Fig. 7(b) is presented in Fig. 7(c), but here the vADCP pulse length is increased to 16 m. Hence the sampling range of each cell is increased to 32 m instead of 8 m. The resampled velocity profile is smoother. The velocity deficit is weaker and over a larger vertical range compared to Fig. 7(b). However, details of the DG wake are lost compared to a lower pulse length. The profile with the higher pulse length correlates better with the observations than the l_{pulse}= 4 m case.

Using the normalized velocity ($\overline{U}(z)_{DG}/\overline{U}(z)_{UD}$), the effects of the DG on the tidal flow can be isolated. The

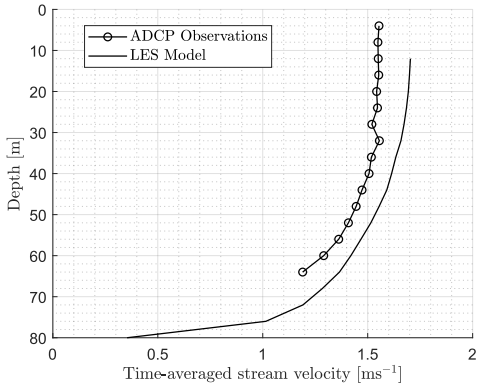

Fig. 7(a). Vertical profile of time-averaged stream velocity component from the ADCP observations, $\bar{u}_o$ and the LES model in the tidal flow (no DG operation). Lower mean flow velocity is seen in the ADCP data compared to the model.

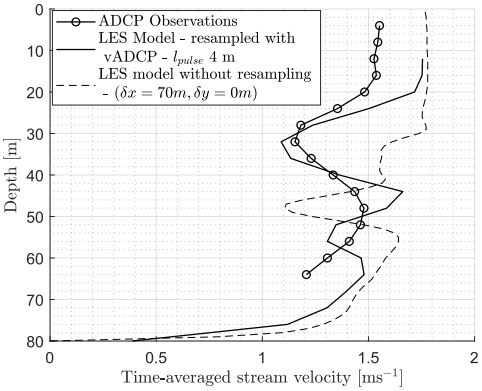

Fig. 7(b). Vertical profile of time-averaged velocity from the ADCP observations and LES model, resampled with a vADCP, when the DG is operational. The profiles are measured at 70 m downstream of the DG wake ($\delta x = 70m$). The LES without resampling at the same location as the vADCP is potted. The resampling is done using vADCP with a l_{pulse} of 4 m, located at $\delta x = 70m, \delta y = 0m$.

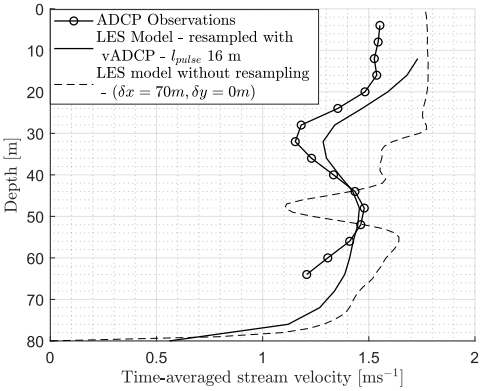

Fig. 7(c). Similar plot as Fig. 6(b), but the resampling is done with a higher pulse length of 16 m. This smoothens the velocity profile and produces a weaker deficit.

subscripts DG and UD stand from Deep Green and Undisturbed tidal flow respectively. In the regions outside the DG trajectory, there is an increase in the flow velocity due to the flow moving around the DG (see Fig. 8). In Fig.8 this effect is seen both in the LES model and the observations. There are two deficit cores in the numerical model data with l_{pulse} = 4m compared to just one in the observations. It could be an effect of the lower mean flow in the observations, that the weaker deficit recovers faster before reaching the ADCP location. This needs to be investigated further with better observation conditions and knowledge of the parameters used in the observations.

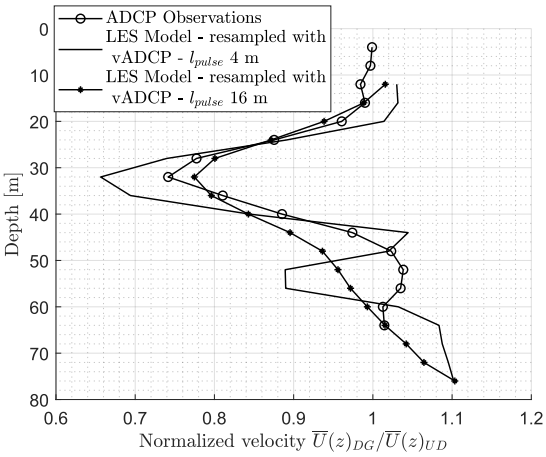

Fig. 8. Vertical profile of normalized velocity ($\overline{U}(z)_{DG}/\overline{U}(z)_{UD}$) i.e., normalizing the DG velocity with the tidal flow velocity. Normalized velocity from the ADCP observations and the LES model, resampled with a l_{pulse} of 4 m and 16 m. Normalizing It isolates the effects of DG on flow

IV. CONCLUSION

The numerical model using LES and ALM was used to simulate a tidal flow and tidal flow with a Deep Green. Comparing the numerical model results without resampling, with observations showed discrepancies hence the numerical model data is resampled using a virtual ADCP. The correlation between the numerical model and the observations improved after the resampling. The numerical model was able to predict the features of the DG wake compared to the observations. Using time-averaged velocities, the effect of the DG on the tidal flow was studied. Effects of the DG on the tidal flow, predicted by the numerical model was comparable to the observations. This indicates that the numerical model can be used for further analysis of tidal power kites (optimization studies, arrays, etc.).

This study also highlights that while making observations of tidal turbine wakes, care should be taken to set desirable beam orientations and pulse lengths. As both have a significant impact on the observational results of the structure of the wake.

Since the beam orientation and the pulse length used in the observations is unknown, there remain some uncertainties but the study acts as a proof of concept for the LES model.

ACKNOWLEDGEMENT

We acknowledge funding from Swedish Energy Agency through project P42247-2. The computations were

enabled by resources provided by the National Academic Infrastructure for Supercomputing in Sweden (NAISS) and the Swedish National Infrastructure for Computing (SNIC) at NSC partially funded by the Swedish Research Council through grant agreements no. 2022-06725 and no. 2018-05973.

REFERENCES

[1] W. Munk and C. Wunsch, "Abyssal recipes II: energetics of tidal and wind mixing," *Deep Sea Research Part I: Oceanographic Research Papers*, vol. 45, no. 12, pp. 1977–2010, Dec. 1998.

[2] D. Magagna and R. Monfardini, "JRC Ocean Energy Status Report 2016 Edition Technology, market and economic aspects of ocean energy in Europe," 2016.

[3] G. Hagerman, B. Polagye, R. Bedard, and M. Previsic, "Methodology for estimating tidal current energy resources and power production by tidal in-stream energy conversion (TISEC) devices," *Stream power feasibility demonstration project, September 29, 2006*, Jan. 2006.

[4] N. O. Jensen, "A note on wind generator interaction ." Risø National Laboratory , Roskilde , 1983.

[5] I. Katic, J. Højstrup, and N. O. Jensen, "A Simple Model for Cluster Efficiency ," *European Wind Energy Association Conference and Exhibition* . A. Raguzzi , Rome , pp. 407-410 BT-EWEC'86. Proceedings. Vol. 1, 1987.

[6] M. J. Churchfield, "A Review of Wind Turbine Wake Models and Future Directions," Boulder, Colorado, 2013.

[7] E. Jump, A. Macleod, and T. Wills, "Review of tidal turbine wake modelling methods: state of the art," *International Marine Energy Journal*, vol. 3, no. 2 SE-Directly submitted articles, pp. 91–100, Sep. 2020.

[8] J. N. Sørensen and W. Z. Shen, "Numerical Modeling of Wind Turbine Wakes," *Journal of Fluids Engineering*, vol. 124, no. 2, pp. 393–399, Jun. 2002.

[9] L. A. Martínez-Tossas, M. J. Churchfield, and S. Leonardi, "Large eddy simulations of the flow past wind turbines: actuator line and disk modeling," *Wind Energy*, vol. 18, no. 6, pp. 1047–1060, 2015.

[10] L. J. Vermeer, J. N. Sørensen, and A. Crespo, "Wind turbine wake aerodynamics," *Progress in Aerospace Sciences*, vol. 39, no. 6–7, pp. 467–510, Aug. 2003.

[11] R. J. Barthelmie *et al.*, "Modelling and measuring flow and wind turbine wakes in large wind farms offshore," *Wind Energy*, vol. 12, no. 5, pp. 431–444, Jul. 2009.

[12] F. Blondel, R. Boisard, M. Milekovic, G. Ferrer, C. Lienard, and D. Teixeira, "Validation and comparison of aerodynamic modelling approaches for wind turbines," *Journal of Physics: Conference Series*, vol. 753, Sep. 2016.

[13] G. Bangga and T. Lutz, "Aerodynamic modeling of wind turbine loads exposed to turbulent inflow and validation with experimental data," *Energy*, vol. 223, p. 120076, 2021.

[14] S. Salunkhe *et al.*, "Validation of Tidal Stream Turbine Wake Predictions and Analysis of Wake Recovery Mechanism," *Journal of Marine Science and Engineering 2019, Vol. 7, Page 362*, vol. 7, no. 10, p. 362, Oct. 2019.

[15] A. Sentchev, M. Thiébaut, and F. Schmitt, "Impact of turbulence on power production by a free-stream tidal turbine in real sea conditions," *Renewable Energy*, vol. 147, pp. 1932–1940, Sep. 2019.

[16] S. T. Fredriksson, G. Broström, M. Jansson, H. Nilsson, and B. Bergqvist, "Large eddy simulation of the tidal power plant deep green using the actuator line method," in *IOP Conference Series: Materials Science and Engineering*, 2017, vol. 276, no. 1.

[17] S. T. Fredriksson, G. Broström, B. Bergqvist, J. Lennblad, and H. Nilsson, "Modelling Deep Green tidal power plant using large eddy simulations and the actuator line method," *Renewable Energy*, vol. 179, pp. 1140–1155, 2021.

[18] P. Bachant, A. Goude, daa-mec, and M. Wosnik, "turbinesFoam/turbinesFoam: v0.1.1," Nov. 2019. https://zenodo.org/record/3542301#.ZCbaUspBxaO

[19] E. De Villiers, "The Potential of Large Eddy Simulation for the Modeling of Wall Bounded Flows Eugene de Villiers," Imperial College London, London, 2006.

[20] C. H. Moeng and P. P. Sullivan, "NUMERICAL MODELS | Large-Eddy Simulation," *Encyclopedia of Atmospheric Sciences: Second Edition*, pp. 232–240, Jan. 2015.

[21] P. Bachant, A. Goude, and M. Wosnik, "Actuator line modeling of vertical-axis turbines," May 2016.

[22] Acoustic Doppler Current Profiler Principles of Operation - A Practical Primer, Teledyne RD Instruments, Inc., P/N 951-6069-00, Jan. 2011

[23] Y. Lu and R. G. Lueck, "Using a Broadband ADCP in a Tidal Channel. Part I: Mean Flow and Shear," *Journal of Atmospheric and Oceanic Technology*, vol. 16, no. 11, pp. 1556–1567, 1999.

[24] Y. Lu and R. G. Lueck, "Using a Broadband ADCP in a Tidal Channel. Part II: Turbulence," *Journal of Atmospheric and Oceanic Technology*, vol. 16, no. 11, pp. 1568–1579, 1999.

[25] S. Frandsen *et al.*, "Analytical modelling of wind speed deficit in large offshore wind farms," *Wind Energy*, vol. 9, no. 1–2, pp. 39–53, Jan. 2006.